



Performance analysis of metal-microheater integrated silicon waveguide phase-shifters

RAMESH K. GUPTA AND BIJOY K. DAS*

*Integrated Optoelectronics Lab / Centre for NEMS and Nanophotonics
Department of Electrical Engineering, IIT Madras, Chennai - 600036, India
bkdas@ee.iitm.ac.in

Abstract: A detailed theoretical and experimental study of metal-microheater integrated silicon waveguide phase-shifters has been carried out. It has been shown that the effective thermal conductance g_w and the effective heat capacitance h_w evaluated per unit length of the waveguide are two useful parameters contributing to the overall performance of a thermo-optic phase-shifter. Calculated values of temperature sensitivity, $S_H = 1/g_w$ and thermal response time, $\tau_{th} = h_w/g_w$ of the phase-shifter are found to be consistent with the experimental results. Thus, a new parameter $\mathcal{F}_H = S_H/\tau_{th} = 1/h_w$ has been introduced to capture the overall figure of merit of a thermo-optic phase-shifter. A folded waveguide phase-shifter design integrated in one of the arms of a balanced MZI switch is shown to be superior to that of a straight waveguide phase-shifter of the same waveguide cross-sectional geometry. The MZI switches were designed to operate in TE-polarization over a broad wavelength range ($\lambda \sim 1550$ nm).

© 2018 Optical Society of America under the terms of the [OSA Open Access Publishing Agreement](#)

1. Introduction

Integrated optical metal-strip microheaters are widely used for reconfigurable silicon photonics devices because of large thermo-optic coefficient of bulk silicon crystal ($dn/dT = 1.86 \times 10^{-4} \text{ K}^{-1}$) [1] and they can be easily implemented using CMOS front-end technology. Some attractive applications of such thermo-optic phase-shifters are reconfigurable wavelength filter [2–4], wavelength interleaver [5], tunable directional coupler [6], large scale optical switch matrix for WDM systems [7–10], etc. In all these examples, metallic microheater strip lines are suitably integrated close to waveguides, acting as waveguide thermo-optic phase-shifters. The thermo-optic phase shift is directly proportional to the temperature rise in the waveguide and its effective length [11]. Again, the temperature rise in the waveguide is proportional to the electrical power dissipated (or consumed as Joule heating) in metallic microheater. Therefore, the power efficiency can be greatly improved by a clever design of waveguide phase-shifter system (waveguide + microheater).

In an integrated optical thermo-optic phase-shifter, the waveguide core is heated typically through the top cladding oxide using metallic (Ti, TiN, CrAu, NiCr, graphene etc.) microheater strip-line integrated directly above the waveguide [12–14]. An attractive meander-type metal microheater design over the oxide cladding of spiraled long waveguide was reported earlier exhibiting lower switching power ($P_\pi = 6.5$ mW) and extremely small switching temperature ($\Delta T_\pi = 0.67\text{K}$) [15]. However, the reported switching time and optical insertion loss in spiraled waveguide section are relatively large ($\tau_{th} = 14$ μs , $IL = 6.5$ dB). Other efforts in switching power reduction were reported by selectively removing the cladding oxide and providing undercuts to the waveguide [16–18]. But this undercut results into a large switching time (few hundreds of microseconds). In contrast, integration of a metallic microheaters directly on the waveguide slab are shown to be relatively faster ($\tau_{th} \sim 5$ μs), but at the cost of large switching power ($P_\pi \sim 50$ mW) [4, 11]. Therefore, it remains a challenging task to design a silicon photonics thermo-optic switch fulfilling all desired features, viz. lower on-state switching power and switching time, compact design for large scale integration, lower optical insertion loss, etc. There

is a little effort seen so far for an optimum design and/or modeling of metallic microheater integrated waveguide phase-shifters. Very recently, Bahadori et al. reported a compact model describing detail dc and transient characteristics of microheater-ring resonator system in silicon photonics platform [19]. Atabaki et al. investigated earlier with numerical simulations followed by experimental demonstration estimating some figure of merits (FOMs) of metallic microheaters used for silicon photonics applications [13]. However, the authors in their model concentrated only on the width of microheater strip-line and the effect of cladding oxide thicknesses. Nevertheless, the FOMs of a thermo-optic phase-shifter (switching power, time and temperature, compactness, optical insertion loss, etc.) can be improved significantly by optimizing the waveguide and microheater design parameters as well as engineering the thermal properties (heat capacitance and thermal conductance) of the system. In this work, we carried out a detailed theoretical analysis of metallic microheater integrated waveguide phase-shifters for the optimizations of above mentioned FOMs. Besides cladding layer, the waveguide cross-sectional geometry and proximity of microheaters are considered for determining the FOMs. The background theory related to all FOMs and necessary numerical simulation results are presented in section 2. In section 3, we have presented the experimental demonstration of Mach-Zehnder interferometer (MZI) thermo-optic switch with a slab-integrated microheater in one of its interferometric arms and validated with theoretically predicted FOMs. The MZI switches were specially designed to operate in TE polarized guided mode over a broad wavelength range ($1520 \text{ nm} \leq \lambda \leq 1630 \text{ nm}$). Finally, concluding remarks comprising of a brief summary of this work and future scopes are given in section 4.

2. Theory and simulation results

For a given waveguide thermo-optic phase-shifter of length L_w , the rise in waveguide temperature for π phase-shift at an operating wavelength λ is given by [15]:

$$\Delta T_\pi \cdot L_w = \frac{\lambda}{2} \cdot \left(\frac{\partial n_{eff}}{\partial T} \right)^{-1} \quad (1)$$

where, n_{eff} is the effective index of the guided mode. Since the value of $\frac{\partial n_{eff}}{\partial T}$ is nearly a constant ($\sim 1.79 \times 10^{-4} \text{ K}^{-1}$ at $\lambda \sim 1550 \text{ nm}$) for silicon photonic wire waveguide, the value of $\Delta T_\pi \cdot L_w$ is also constant ($\sim 4.33 \times 10^3 \text{ K} \cdot \mu\text{m}$). Thus the operating range of differential temperature in the waveguide can be kept lower by simply increasing waveguide length as described by Densmore et al. [15]. Further, the steady-state temperature rise (ΔT_s) in waveguide core is directly proportional to the Joule heating power consumption by a resistive/metallic microheater. The thermal sensitivity S_H of the phase shifter can be defined as [4]:

$$\Delta T_s = S_H \cdot p_w \quad (2)$$

where p_w is the Joule heating power consumption by the microheater normalized to unit length of the waveguide phase-shifter. Thus the higher value of S_H ensures lower power consumption and/or shorter length of the waveguide phase-shifter for a desired phase-shift of the guided mode, but at the cost of higher operating temperature.

On the other hand, the transient rise in waveguide temperature $\Delta T(t)$ can be expressed as:

$$\Delta T(t) = \Delta T_s (1 - e^{-t/\tau_{th}}) \quad (3)$$

In the above equation, the thermal response time is defined by $\tau_{th} = \mathcal{H}/\mathcal{G}$, where \mathcal{H} is the thermal capacity and \mathcal{G} is the conductance of the waveguide-microheater system. Since these parameters depend on waveguide core and cladding materials, waveguide cross-sectional geometry, microheater positioning relative to waveguide core, etc., the value of τ_{th} can be

estimated numerically by solving Fourier's heat equation using FDTD method. However, for a given waveguide phase-shifter, one can estimate waveguide characteristic thermal parameters $h_w (= \mathcal{H}/L_w)$ and $g_w (= \mathcal{G}/L_w)$. Thus we can redefine the response time of a thermo-optic phase-shifter as:

$$\tau_{th} = \frac{h_w}{g_w} \quad (4)$$

Further, for a steady-state temperature rise of ΔT_s of the waveguide-microheater system, the required electrical power is given by $P_e = \Delta T_s \cdot \mathcal{G}$. This again boils down to $p_w = \Delta T_s \cdot g_w$ according to our definitions. Thus Eq. (2) reduces to:

$$S_H \cdot g_w = 1 \quad (5)$$

It is now obvious that for an efficient design of thermo-optic waveguide phase-shifter, we must assure higher thermal sensitivity S_H and lower thermal response time τ_{th} . Therefore, the corresponding figure of merit (\mathcal{F}_H) may be expressed as:

$$\mathcal{F}_H = \frac{S_H}{\tau_{th}} = \frac{\Delta T_s \cdot L_w}{P_e \cdot \tau_{th}} = \frac{1}{h_w} \Rightarrow \mathcal{F}_H \cdot h_w = 1 \quad (6)$$

Higher the value of S_H , one can ensure a shorter design of waveguide phase-shifter. In other words, a compact and efficient thermo-optic waveguide phase-shifter can be designed by simultaneously achieving lower effective thermal conductance g_w and lower effective heat capacity h_w . Moreover, close proximity of microheater to the waveguide core ensures higher value of S_H . However, one must take care about additional optical attenuation of the guided mode due its evanescent tail overlap with the metallic microheater.

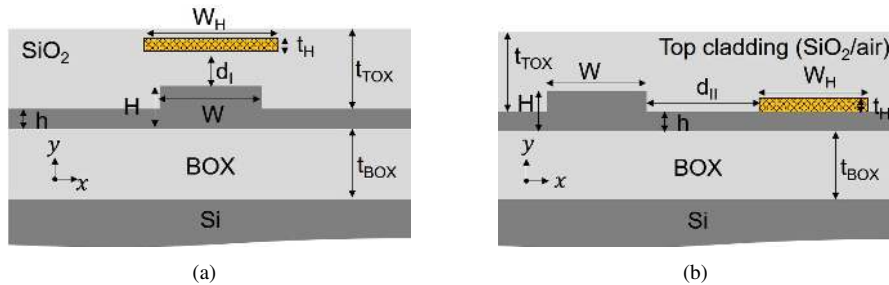


Fig. 1. Schematic cross sectional views of two thermo-optic waveguide phase-shifter architectures along with important design parameters: (a) microheater integrated within top-oxide cladding directly above the waveguide, and (b) microheater directly integrated on the slab of the waveguide beneath the top oxide/air cladding. H - device layer thickness, W - waveguide width, h - silicon slab thickness remain after waveguide definition, W_H - microheater width, t_H - microheater thickness, and $d_{I,II}$ - gap between waveguide and microheater.

For performance analysis, we have considered two different waveguide microheater configurations, commonly used for integrated optical thermo-optic phase-shifter in SOI platform as shown in Fig. 1. According to Atabaki et al., the two configurations shown in Fig. 1(a) and Fig. 1(b) are categorized as Type-I and Type-II architectures, respectively [20]. It was shown with detail analyses that the Type-II microheaters are superior than that of Type-I microheaters in terms of thermal response time of a micro-disk resonator. To analyze the performance of a Type-I or Type-II waveguide phase-shifter, we need to consider waveguide parameters like width W , slab height h , and the lateral distances of microheater to waveguide d_I (d_{II}) for Type-I (Type-II) as

defined in the figures. The width ($W_H = 1 \mu\text{m}$) and thickness ($t_H = 100 \text{ nm}$) of a Ti metallic microheater strip are assumed same for both types of architectures. Moreover, following the standards of silicon photonics foundries, we have considered device layer thickness of $H = 220 \text{ nm}$ and BOX layer (SiO_2) thickness of $t_{BOX} = 2 \mu\text{m}$.

For a given design of SOI waveguide geometry (W , H , and h) discussed above, the thermal properties (thermo-optic efficiency and response time) of the waveguide phase-shifter are mainly determined by the waveguide slab layer thickness h , lateral distance of microheater d_I or d_{II} and top cladding material SiO_2 or Air. Therefore, it is important to estimate the valid range of W and h for single-mode guidance over a desired wavelength range ($\lambda \sim 1550 \text{ nm}$). We have simulated allowed guided modes and their polarizations by varying W (300 nm to 700 nm) and h (0 to 200 nm) using Lumerical's MODE Solutions separately for SiO_2 and air top-cladding layers (see Fig. 2).

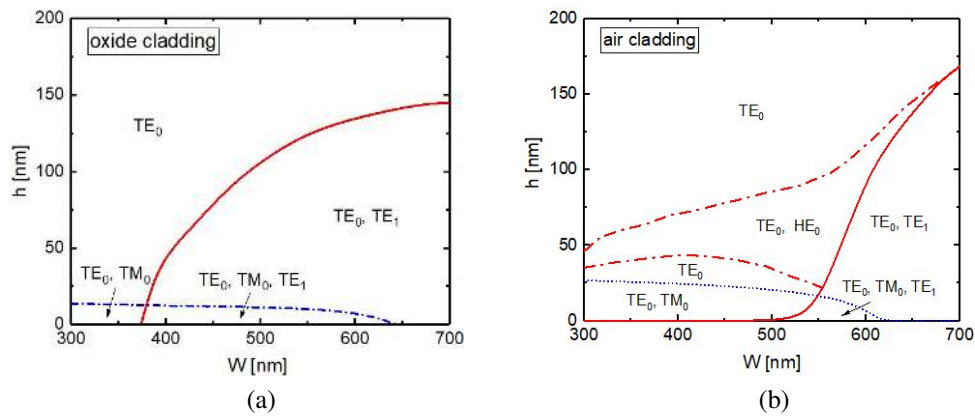


Fig. 2. Allowed guided modes (TE_0 , TE_1 , TM_0 and HE_0) are shown in W - h plane for: (a) oxide top-cladding (b) air top-cladding. The calculations are carried out for $H = 220 \text{ nm}$, and $t_{BOX} = t_{TOX} = 2 \mu\text{m}$ at an operating wavelength $\lambda = 1550 \text{ nm}$.

The degree of polarization of the guided modes are defined by comparing the fraction of transverse electric field component along x-direction:

$$\Gamma_x = \frac{\int |E_x|^2 dx dy}{\int (|E_x|^2 + |E_y|^2) dx dy} \quad (7)$$

where, E_x and E_y are the transverse electric field components of a guided mode. For convenience, we have assumed a guided mode to be TE -polarized if $\Gamma_x \geq 0.6$, TM -polarized if $\Gamma_x \leq 0.4$ and hybrid or HE -polarized for $0.4 < \Gamma_x < 0.6$; and accordingly demarcated in Figs. 2(a) and 2(b) as a function of W and h for a given $H = 220 \text{ nm}$. Besides single-mode guiding condition, we also observe that TE_0 mode is supported for all values of h when W is kept below 375 nm (500 nm) for air (SiO_2) top-cladding. Both TE_0 and TM_0 modes are supported for $h \leq 15 \text{ nm}$ (30 nm) for oxide (air) top-cladding.

In order to investigate thermo-optic FOMs like S_H and τ_{th} , we have considered TE_0 mode guidance in waveguides with $W = 350 \text{ nm}$ and $0 \leq h \leq 200 \text{ nm}$ for both Type-I and Type-II architectures. The important properties of core Si, cladding SiO_2 , and microheater Ti-strip used for numerical simulation are given in Table 1. The thickness dependent thermal conductivities [23] were appropriately considered for solving the heat transport equation [25] using COMSOL

Table 1. The values of various thermal and electrical parameters like specific heat capacity (c_v), material mass density (ρ_m), thermal conductivity (κ), electrical conductivity (σ), thermal expansion coefficient (α_c), refractive index (n) used for Ti, Si and SiO₂ in calculating thermo-optic effects. They are either taken as default values from the library of COMSOL Multiphysics simulator or from available literatures [21–24].

Property	Ti	Si	SiO ₂
c_v [J/(Kg.K)]	544	700	730
ρ_m [kg/m ³]	4506	2329	2200
κ [W/(m.K)]	21.9	15-140	1.4
σ [S/m]	2.6×10^6	8.7	10^{-15}
α_c [1/K]	8.6×10^{-6}	2.6×10^{-6}	0.5×10^{-6}
n ($\lambda \sim 1550$ nm)	3.6848 + j4.6088	3.4447	1.444

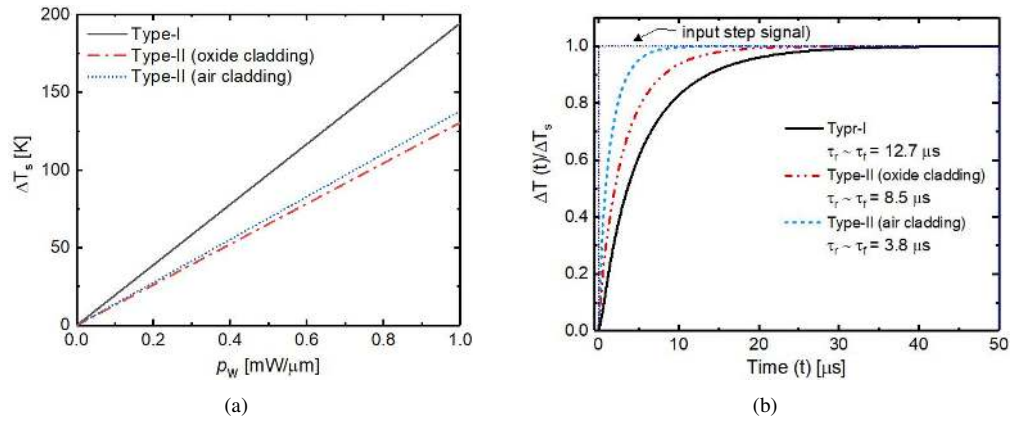


Fig. 3. Simulation results for estimating thermal sensitivity S_H and response time τ_{th} for Type-I, Type-II (oxide cladding), and Type-II (air cladding) waveguide phase-shifters (see text for design parameters): (a) calculated steady-state temperature rise (ΔT_s) of the waveguide core as a function of electrical power dissipation per unit length of waveguide phase-shifter, and (b) transient temperature rise $\Delta T(t)$ normalized to ΔT_s as a function time for a unit step-function excitation of input voltage signal to the microheaters.

Multiphysics [21] with appropriate boundary conditions at the interfaces as described in Ref. [13]. To start with, we have simulated the steady-state values of temperature rise (ΔT_s) at the waveguide core ($W = 350$ nm, $H = 220$ nm, $h = 100$ nm) as a function of electrical power dissipation per unit length (p_w) of waveguide due to positioning of Ti strip microheaters ($W_H = 1 \mu$ m and $t_H = 100$ nm) at $d_I = d_{II} = 1 \mu$ m. As expected, the ΔT_s vs. p_w plots shown in Fig. 3(a) are following the linear relationship as defined in Eq. (2). It is evident that the sensitivity S_H for Type-I architecture (195 K· μ m/mW) is reasonably higher than that of Type-II architectures (~ 130 K· μ m/mW). This is expected due to the large thermal conductivity of silicon slab ($h = 100$ nm) which increases the effective thermal conductance (g_w) of the slab-heating configuration and hence S_H reduces [Eq. (5)] compared to oxide-heating. However, it is also observed that the value of S_H for Type-II (air cladding) is slightly higher than that of Type-II (oxide cladding). This is attributed to the lower thermal conductivity of air cladding than that of SiO₂. The transient response of the temperature

rise $\Delta T(t)$ in the waveguide core is evaluated by exciting the microheater with a step input voltage signal at $t = 0$. The simulated results (with ΔT_s normalized to unity) for the above mentioned Type-I and Type-II architectures are shown in Fig. 3(b). The thermal response time τ_{th} estimated for Type-I, Type-II (oxide cladding), and Type-II (air cladding) are 12.7 μs , 8.5 μs , and 3.8 μs , respectively. Thus the above simulation results confirm that top oxide cladding results into an effective decrease of thermal conductance (g_w) and/or effective increase of thermal capacitance (h_w). The proximity of microheater to the waveguide core also play a role in reducing the value of τ_{th} as well as increasing S_H .

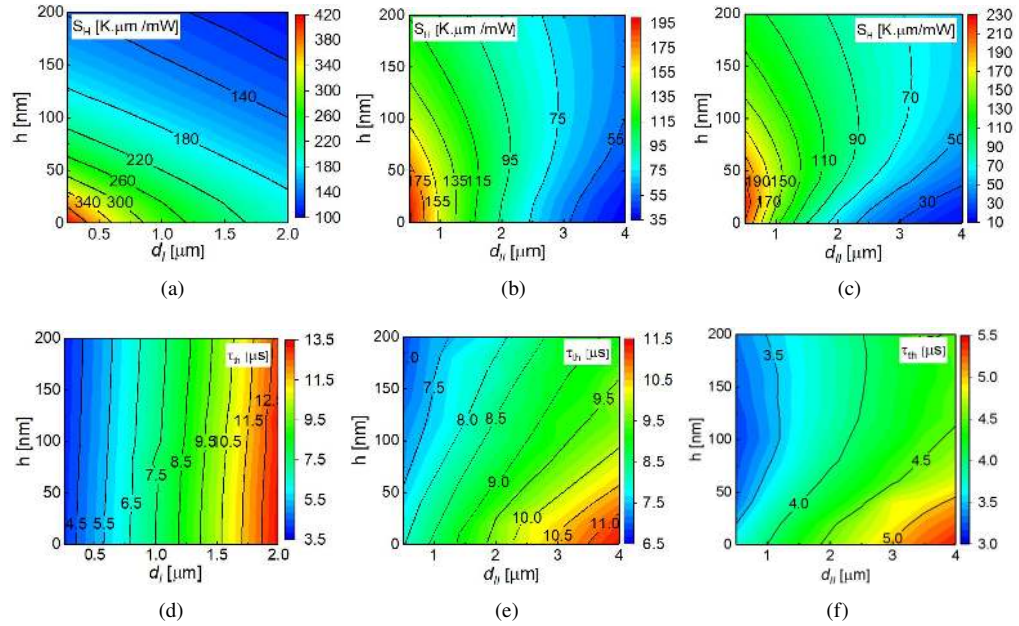


Fig. 4. Contour plots of S_H in $\text{K}\cdot\mu\text{m}/\text{mW}$ and τ_{th} in μs calculated as a functions of $d_{I,II}$ and h for Type-I (a and d), Type II oxide cladding (b and e) and Type-II air cladding (c and f) heater architectures. The calculations were carried out for TE_0 guided mode at $\lambda = 1550$ nm ($W = 350$ nm and $H = 220$ nm).

A more detail simulation results for S_H and τ_{th} as a function of both h and d_I or d_{II} are shown in color contour plots in Fig. 4. Note that, irrespective of the heater configuration (oxide-heating or slab heating), S_H reduces with $d_{I,II}$ and h because of the increase in effective thermal conductance (g_w). In contrast, τ_{th} increases with $d_{I,II}$. Though g_w of the system increases with h , the value of τ_{th} remains unaffected w.r.t. h for oxide-heating, since the waveguide core is heated right from the top at a constant distance of d_I . We notice that the value of S_H can be as high as $> 350 \text{ K}\cdot\mu\text{m}/\text{mW}$ and τ_{th} is as low as $< 4.5 \mu\text{s}$ for a Type-I configuration with $h < 25$ nm and $d_I < 250$ nm. On the other hand, they are $> 190 \text{ K}\cdot\mu\text{m}/\text{mW}$ ($> 220 \text{ K}\cdot\mu\text{m}/\text{mW}$) and $< 8.0 \mu\text{s}$ ($< 4 \mu\text{s}$) for a oxide clad (air clad) Type-II configuration with $h < 50$ nm and $d_{II} < 500$ nm. Thus the studies help for maximizing the figure of merit \mathcal{F}_H of the waveguide phase-shifter defined by S_H/τ_{th} . In doing so, one needs to minimize the value of d_I or d_{II} . However, closer proximity of metal microheater to the waveguide introduces optical attenuation of the guided mode because of plasma dispersion effect through evanescent field overlap. We have numerically estimated (using Lumerical's MODE Solutions) the optical loss coefficient (α_h) for TE_0 guided mode as a function of $d_{I,II}$ (considering h as a parameter) with complex refractive index of Ti-strip ($W_H = 1 \mu\text{m}$, $t_H = 100$ nm) as $3.6848 + j4.6088$ at $\lambda = 1550$ nm [24]. This has been shown in Figs. 5(a) and 5(b) for Type-I and Type-II (oxide cladding and air cladding), respectively. As expected,

α_h (expressed in dB/mm) increases as the value of d_I or d_{II} decreases. However, for type-II configuration (with a given d_{II}), α_h increases with slab height due to poor confinement of the optical mode inside waveguide core. Whereas, for Type-I (with a given d_I), the evanescent field-strength along y direction reduces with h and hence α_h reduces. It must be noted that the α_h is nearly same for oxide cladding and air cladding in Type-II configuration. Nevertheless, the metallic losses are negligibly small ($\alpha_h < 0.1$ dB/mm) for $d_{I,II} > 0.5$ μm .

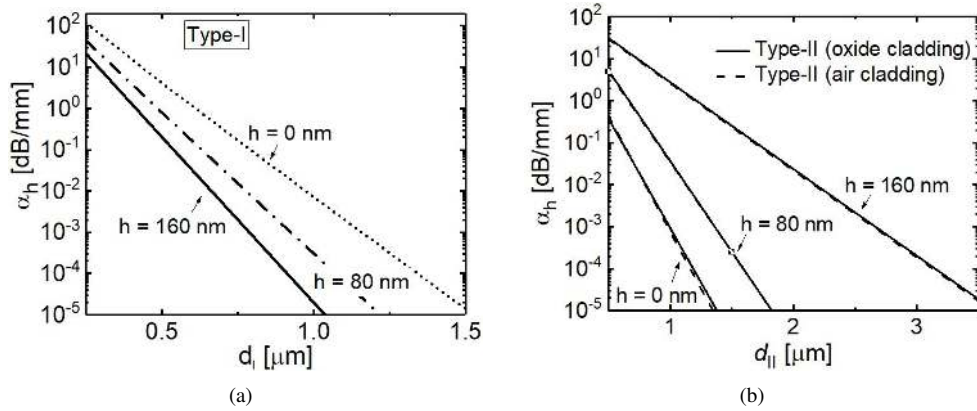


Fig. 5. Calculated optical loss coefficient α_h of TE_0 mode in dB/mm ($\lambda = 1550$ nm) due to interaction between evanescent field and metallic microheater as a function of d_I for Type-I and d_{II} for Type II with h as a parameter: (a) Type-I and (b) Type-II (oxide cladding and air cladding). The calculations are carried out for $W = 350$ nm and $H = 220$ nm.

It is worth mentioning here that we have restricted our above numerical studies for a straight waveguide phase-shifter where both waveguide and metallic microheater strip-line are parallel to each other for both Type-I and Type-II architectures. However, one can extend this study to spiraled waveguide geometry and meander-type metallic microheater in Type-I configurations as described in Ref. [15]. From their experimental results, we estimate the value of S_H as large as ~ 640 K $\cdot\mu\text{m}/\text{mW}$. Similarly, for a bend or folded waveguide (and microheater) design in Type-II configuration, the value of S_H can be enhanced significantly. This has been validated with numerical simulations as well as experimental results described in following section.

3. Experimental results and discussion

The theoretical model discussed above has been validated with experimental results by integrating Type-II (air cladding) phase-shifters in one of the arms of balanced MZIs fabricated in SOI platform (device layer ~ 220 nm, BOX layer ~ 2 μm). The MZIs were designed with wavelength independent directional couplers (WIDCs) for switching operation over a broad wavelength range (operating at $\lambda \sim 1550$ nm) as described in Ref. [26]. The waveguides were designed with $W = 350$ nm and $h = 160$ nm, supporting only TE_0 -polarized guided mode for the above mentioned desired wavelength range. The passive MZI structures and reference waveguides were fabricated using electron beam lithography (EBL) followed by inductively coupled plasma reactive ion etching process (ICPRIE). Afterwards, contact pads (Al) and microheater (Ti) both were patterned one after another using EBL and subsequent lift-off process. Detailed fabrication process parameters of MZI and microheater can be found elsewhere [4, 27]. For device characterizations, the input/output waveguides are terminated with broadband grating couplers of bandwidth ~ 70 nm, as described in [27].

For a comparative study, two different types of MZIs were fabricated; the first type has straight

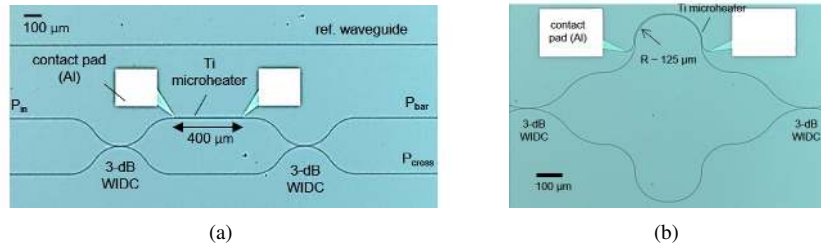


Fig. 6. Microscopic images of the fabricated MZI based 2×2 thermo-optic switches integrated with Type-II (air cladding) waveguide phase-shifter: (a) straight-waveguide phase-shifter integrated MZI (S-MZI), and (b) folded waveguide phase-shifter integrated MZI (F-MZI).

waveguide phase-shifters (S-MZI), whereas the second type has folded waveguide phase-shifters (F-MZI). Both straight and folded waveguide phase-shifters have same length $L_H = 400 \mu\text{m}$, $d_{II} \sim 3 \mu\text{m}$, $W_H \sim 1 \mu\text{m}$, and $t_H \sim 100 \text{nm}$. The microscopic images of both types of fabricated MZIs are shown in Fig. 6. The line resistance of fabricated microheaters is estimated as $r_H \sim 70 \Omega/\mu\text{m}$ and the resistance of two flaring regions including the probe contact resistance is extracted as $\sim 4 \text{k}\Omega$ (R_{CH}). Thus for a waveguide microheater of length L_H used for above mentioned MZI switch, the actual electrical power consumption for thermo-optic switching experiments for all fabricated devices: $P_e = I^2 r_H L_H$, where I is the *dc* or *rms* value of current through the microheater. As the length of microheaters is kept relatively long ($L_H = 400 \mu\text{m}$), the effective phase-shifter length $L_{eff} \approx L_H = L_w$ as it was modeled earlier in Ref. [11]. Moreover, for a waveguide phase-shifter of length $L_w \approx 400 \mu\text{m}$, the value of ΔT_π calculated using Eq. (1) is found to be small ($\sim 11\text{K}$) and hence the temperature dependent change in microheater resistance is assumed to be insignificant during switching operation.

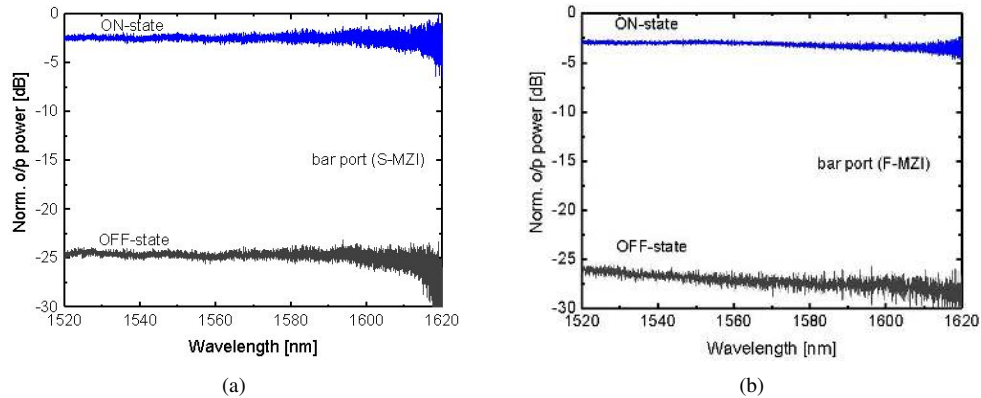


Fig. 7. Wavelength independent transmission characteristics at the bar ports measured for ON-state (maximum transmission) and OFF-state (minimum transmission) switching power levels: (a) S-MZI, and (b) F-MZI.

For thermo-optic switching characterizations of fabricated devices, we used two fiber-optic probes for input and output light coupling via grating couplers (GCs) and simultaneously two electrical probes for driving the microheater. A high resolution spectrum analyzer (APEX 2043B) with inbuilt CW laser source ($1520 \text{ nm} \leq \lambda \leq 1620 \text{ nm}$) was used for the experiment. The

microheaters were sourced by connecting terminal Al contact pads with a current source measuring unit (SMU). The experimental set-up for studying thermo-optic switching characteristics of fabricated devices may be found elsewhere [4]. The wavelength dependent transmission characteristics for both ON-state and OFF-state at the bar ports ($1520 \text{ nm} \leq \lambda \leq 1620 \text{ nm}$) normalized with a reference waveguide transmission (to eliminate wavelength dependent fiber to input/output grating coupler losses) are shown in Figs. 7(a) and 7(b) corresponding to an S-MZI and an F-MZI, respectively. A wavelength independent insertion loss of $\sim 2.5 \text{ dB}$ is recorded for

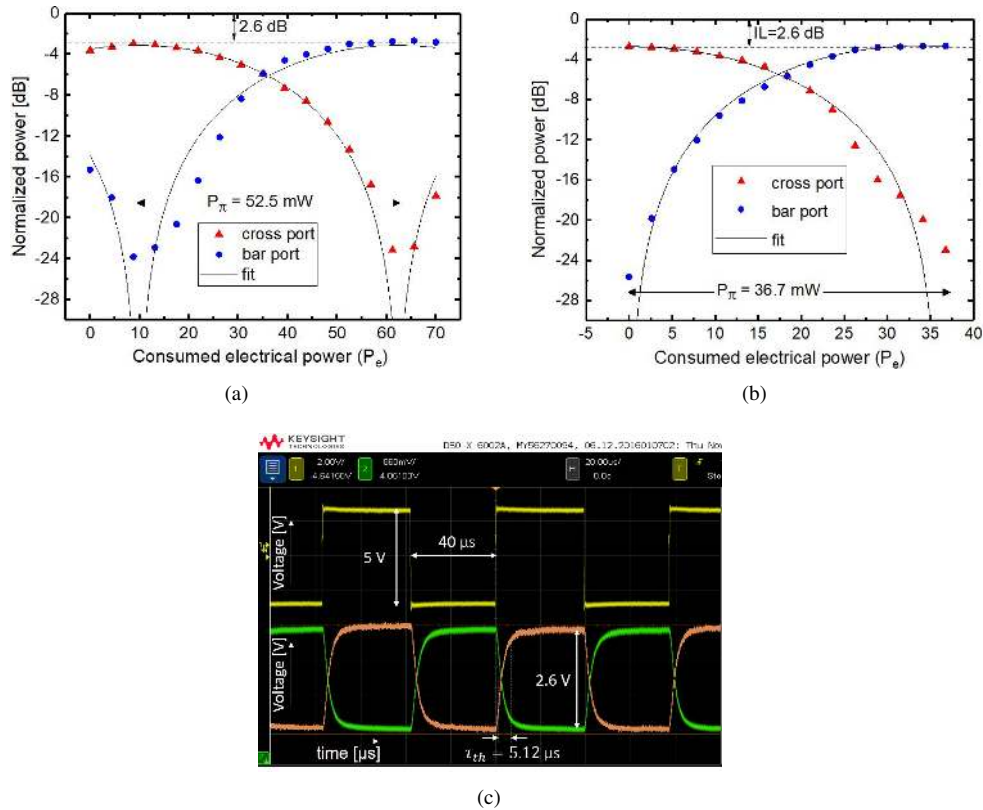


Fig. 8. Switching characteristics measured at $\lambda = 1550 \text{ nm}$: (a) transmission at cross and bar ports of an S-MZI, (b) transmission at cross and bar ports of an F-MZI, and (c) transient characteristics measured at bar and cross ports of an S-MZI with the microheater driven by a square pulse (identical transient characteristics for F-MZI).

both S-MZI and F-MZI switches, which is mainly attributed to the total insertion loss of two 3-dB power splitters. The observed oscillations at longer wavelengths may be attributed to the weaker coupling efficiency of the grating couplers resulting into noise level detection limit of the photodetector. Typical electrical power required for switching optical signal from cross port to the bar port (with an extinction of $> 20 \text{ dB}$) is $P_e \sim 52.5 \text{ mW}$ ($\sim 36.7 \text{ mW}$) for fabricated S-MZI (F-MZI) switches. In case of folded waveguide microheater, heat is dissipated more effectively in the smaller volume, compared to that of straight waveguide microheater of same length. The steady-state transmitted optical signal ($\lambda = 1550 \text{ nm}$) at the bar and cross ports of the above mentioned S-MZI and F-MZI as a function of electrical power dissipated/consumed by the microheaters are shown in Figs. 8(a) and 8(b), respectively. Though both types of MZIs were designed with balanced arms, a little mismatch occasionally observed for some fabricated

devices. For example, an additional bias electrical power of $P_e = 8.75$ mW was required for achieving maximum (minimum) transmission at the cross (bar) port of the S-MZI. Typical transient response of optical transmission at both bar- and cross-ports of the MZI switch (straight or folded microheater) are shown in Fig. 8(c). This has been obtained for an input modulating voltage of 5 V peak to peak at a repetition rate of 12 kHz superimposed with a dc biasing voltage across the curved waveguide microheater. The recorded rise/fall time for both types of microheaters are measured to be nearly same (~ 5 μ s) which is higher than the theoretical calculation (4.2 μ s) as shown in Fig. 4(f). This deviation may be due to the assumption of lower value of thermal conductivities and/or higher values of heat capacitances (for both core and claddings) in theoretical simulation.

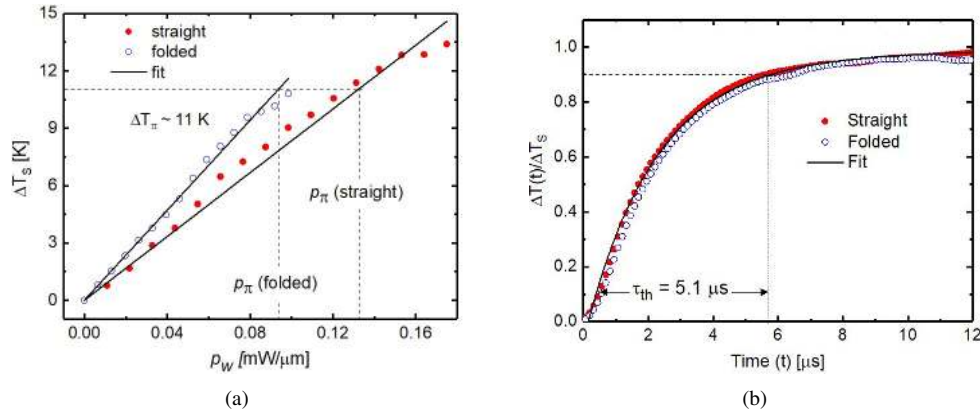


Fig. 9. Steady-state and transient temperature characteristics of straight and folded waveguide phase-shifters used in S-MZI and F-MZI, respectively: (a) extracted steady-state temperature ΔT_s in the waveguide core as a function of dissipated electrical power per unit length of the phase-shifter (p_w), and (b) extracted transient temperature $\Delta T(t)$ in the waveguide core as a function of time t .

The steady-state switching characteristics obtained for S-MZI and F-MZI are fitted with appropriate analytical transfer functions [4] and we have extracted the values of ΔT_s (steady-state temperature in the waveguide core) vs. p_w (electrical power consumed per unit length of a waveguide phase-shifter) for both straight and folded waveguide phase-shifters as shown in Fig. 9(a). The slope of ΔT_s vs. p_w is a measure of the sensitivity figure of merit S_H of the waveguide phase-shifter as defined earlier. The value of S_H extracted for an S-MZI is 82.4 K $\cdot\mu$ m/mW, which is slightly higher than that of theoretical prediction of 73.5 K $\cdot\mu$ m/mW. This may be attributed to the fact of our assumption $L_w = L_H$; a correction term is required for $L_w = L_{eff} = L_H + \Delta$, where $\Delta \sim 10$ μ m for $L_H > 100$ μ m [11]. In other words, the effective conductance (g_w) of fabricated devices is slightly lower than that of theoretical calculations which is consistent with the observed higher values of thermal response time (τ_{th}) of the fabricated devices discussed earlier. Nevertheless, we observed a significantly enhanced value of $S_H = 119$ K $\cdot\mu$ m/mW in case of folded waveguide phase-shifter as predicted earlier. The transient characteristics obtained for S-MZI and F-MZI are again fitted with the corresponding analytical functions to extract the temperature rise $\Delta T(t)$ in the waveguide core of the phase-shifters [see Fig. 9(b)]; both straight and folded waveguide phase-shifters are shown to be following Eq. (3) with $\tau_{th} = 5.1$ μ s. Thus the experimentally observed value of \mathcal{F}_H in a folded waveguide phase-shifter (23.3 K $\cdot\mu$ m/mW $\cdot\mu$ s) is about 1.5 times higher than that of a straight waveguide phase-shifter (16.2 K $\cdot\mu$ m/mW $\cdot\mu$ s) for our fabricated devices. It is possible to improve the value of \mathcal{F}_H further by designing more tightly folded waveguide phase-shifter with close proximity of microheater

but one needs to take care of associated optical losses of the guided mode. Using Eqs. (5) and (6), we have extracted the thermal characteristic parameters g_w and h_w as 1.21×10^{-2} mW/K· μm (1.21×10^{-2} mW/K· μm) and 6.17×10^{-2} mW· μs /K· μm (4.29×10^{-2} mW· μs /K· μm), respectively, for the fabricated straight (folded) design waveguide phase-shifters in Type-II (air cladding) architecture.

4. Conclusions

In summary, a theoretical model for the performance analysis of a metallic strip-line microheater integrated waveguide phase-shifter has been developed. The model helps to define two important figure of merits such as temperature sensitivity S_H and $\mathcal{F}_H (= S_H/\tau_{th})$ following thumb-rules of $S_H \cdot g_w = 1$ and $\mathcal{F}_H \cdot h_w = 1$, respectively, where g_w and h_w are characteristic line conductance and line heat capacitance of the waveguide phase-shifter. These figure of merits were calculated for SOI waveguides (supporting TE_0 guided mode) integrated with Type-I and Type-II microheater architectures. It has been shown by numerical simulation that Type-II microheaters offer faster switching time than that of Type-I microheaters. It has been also shown that both S_H and \mathcal{F}_H can be improved significantly by proper choices of waveguide design parameters, closer proximity of microheater to the waveguide core, and suitably folding the waveguide-microheater phase-shifter system. However, care must be taken to limit the bend induced waveguide loss and loss due to evanescent field overlap with metallic microheater. The theoretical model is further validated with experimental results by fabricating 2×2 MZI switches (wavelength independent) designed with Type-II microheaters in SOI platform. Though the demonstrated MZI switches were not designed with the best possible values of figure of merits (S_H , τ_{th} and \mathcal{F}_H), the experimental technique described here helps to extract the characteristic parameters like g_w and h_w of a thermo-optic waveguide phase-shifter for its modeling and optimized design.

References

1. G. Cocorullo and I. Rendina, "Thermo-optical modulation at 1.5 μm in silicon etalon," *Electron. Lett.* **28**, 83–85 (1992).
2. H. Shen, M. H. Khan, L. Fan, L. Zhao, Y. Xuan, J. Ouyang, L. T. Varghese, and M. Qi, "Eight-channel reconfigurable microring filters with tunable frequency, extinction ratio and bandwidth," *Opt. Express* **18**, 18067–18076 (2010).
3. J. Tao, H. Cai, Y. Gu, and A. Liu, "Demonstration of a compact wavelength tracker using a tunable silicon resonator," *Opt. Express* **22**, 24104–24110 (2014).
4. R. Sumi, R. K. Gupta, N. DasGupta, and B. K. Das, "Ultra-broadband add-drop filter/switch circuit using subwavelength grating waveguides," *IEEE J. Sel. Top. Quantum Electron.* **25**, 1–11 (2019).
5. L.-W. Luo, S. Ibrahim, A. Nitkowski, Z. Ding, C. B. Poitras, S. B. Yoo, and M. Lipson, "High bandwidth on-chip silicon photonic interleaver," *Opt. Express* **18**, 23079–23087 (2010).
6. P. Orlandi, F. Morichetti, M. J. Strain, M. Sorel, A. Melloni, and P. Bassi, "Tunable silicon photonics directional coupler driven by a transverse temperature gradient," *Opt. Lett.* **38**, 863–865 (2013).
7. K. Tanizawa, K. Suzuki, M. Toyama, M. Ohtsuka, N. Yokoyama, K. Matsumaro, M. Seki, K. Koshino, T. Sugaya, S. Suda, G. Cong, T. Kimura, K. Ikeda, S. Namiki, and H. Kawashima, "Ultra-compact 32×32 strictly-non-blocking Si-wire optical switch with fan-out LGA interposer," *Opt. Express* **23**, 17599–17606 (2015).
8. K. Suzuki, K. Tanizawa, S. Suda, H. Matsuura, T. Inoue, K. Ikeda, S. Namiki, and H. Kawashima, "Broadband silicon photonics 8×8 switch based on double-Mach-Zehnder element switches," *Opt. Express* **25**, 7538–7546 (2017).
9. C. Li, W. Zheng, P. Dang, C. Zheng, Y. Wang, and D. Zhang, "Silicon-microring-based thermo-optic non-blocking four-port optical router for optical networks-on-chip," *Opt. Quantum Electron.* **48**, 552 (2016).
10. M. S. Dahlem, C. W. Holzwarth, A. Khilo, F. X. Kärtner, H. I. Smith, and E. P. Ippen, "Reconfigurable multi-channel second-order silicon microring-resonator filterbanks for on-chip WDM systems," *Opt. Express* **19**, 306–316 (2011).
11. S. Kaushal and B. K. Das, "Modeling and experimental investigation of an integrated optical microheater in silicon-on-insulator," *Appl. Opt.* **55**, 2837–2842 (2016).
12. X. Wang, J. A. Martinez, M. S. Nawrocka, and R. R. Panepucci, "Compact thermally tunable silicon wavelength switch: modeling and characterization," *IEEE Photon. Technol. Lett.* **20**, 936–938 (2008).
13. A. Atabaki, E. S. Hosseini, A. Eftekhari, S. Yegnanarayanan, and A. Adibi, "Optimization of metallic microheaters for high-speed reconfigurable silicon photonics," *Opt. Express* **18**, 18312–18323 (2010).
14. D. Schall, M. Mohsin, A. A. Sagade, M. Otto, B. Chmielak, S. Suckow, A. L. Giesecke, D. Neumaier, and H. Kurz, "Infrared transparent graphene heater for silicon photonic integrated circuits," *Opt. Express* **24**, 7871–7878 (2016).

15. A. Densmore, S. Janz, R. Ma, J. H. Schmid, D.-X. Xu, A. Delâge, J. Lapointe, M. Vachon, and P. Cheben, "Compact and low power thermo-optic switch using folded silicon waveguides," *Opt. Express* **17**, 10457–10465 (2009).
16. P. Sun and R. M. Reano, "Free-standing silicon-on-insulator strip waveguides for submilliwatt thermo-optic switches," in *Frontiers in Optics*, (Optical Society of America, 2010), p. FMH3.
17. Q. Fang, J. F. Song, T.-Y. Liow, H. Cai, M. B. Yu, G. Q. Lo, and D.-L. Kwong, "Ultralow power silicon photonics thermo-optic switch with suspended phase arms," *IEEE Photon. Technol. Lett.* **23**, 525–527 (2011).
18. Z. Lu, K. Murray, H. Jayatileka, and L. Chrostowski, "Michelson interferometer thermo-optic switch on soi with a 50- μ W power consumption," in *Photonics Conference (IPC), 2016 IEEE*, (IEEE, 2016), pp. 107–110.
19. M. Bahadori, A. Gazman, N. Janosik, S. Rumley, Z. Zhu, R. Polster, Q. Cheng, and K. Bergman, "Thermal rectification of integrated microheaters for microring resonators in silicon photonics platform," *J. Light. Technol.* **36**, 773–788 (2018).
20. A. H. Atabaki, A. A. Eftekhar, S. Yegnanarayanan, and A. Adibi, "Sub-100-nanosecond thermal reconfiguration of silicon photonic devices," *Opt. Express* **21**, 15706–15718 (2013).
21. "COMSOL Multiphysics version 5.3," <https://www.comsol.com>.
22. B. Singh and N. Surplice, "The electrical resistivity and resistance-temperature characteristics of thin titanium films," *Thin Solid Films* **10**, 243–253 (1972).
23. M. Asheghi, M. Touzelbaev, K. Goodson, Y. Leung, and S. Wong, "Temperature-dependent thermal conductivity of single-crystal silicon layers in SOI substrates," *J. Heat Transf.* **120**, 30–36 (1998).
24. P. Johnson and R. Christy, "Optical constants of transition metals: Ti, Cr, Mn, Fe, Co, Ni, and Pd," *Phys. Rev. B* **9**, 5056 (1974).
25. F. Kreith, R. M. Manglik, and M. S. Bohn, *Principles of Heat Transfer* (Cengage Learning, 2012).
26. R. K. Gupta, S. Chandran, and B. K. Das, "Wavelength independent directional couplers for integrated silicon photonics," *J. Light. Technol.* **22**, 4916–4923 (2017).
27. S. Chandran, R. K. Gupta, and B. K. Das, "Dispersion enhanced critically coupled ring resonator for wide range refractive index sensing," *IEEE J. Sel. Top. Quantum Electron.* **23**, 424–432 (2017).